Frequency effects on lift and drag for flow past an oscillating cylinder

Z.C. Zheng*, N. Zhang

Department of Mechanical and Nuclear Engineering, Kansas State University, Manhattan, Kansas 66506, USA

Abstract

A transversely oscillating cylinder in a uniform flow is modeled to investigate frequency effects of flow-induced wake on lift and drag of the cylinder. Specifically, verified unsteady fluid dynamic simulations using an immersed-boundary method in a fixed Cartesian grid predict the flow structure around the cylinder and reveal how the integration of surface pressure and shear distributions provides lift and drag on the oscillating cylinder. In this study, frequency ranges to be considered are both near and away from the natural frequency of wake vortex shedding. Subsequently, the effects of frequency lock-in, superposition and demultiplication on lift and drag are discussed based on the spectral analysis of time histories of lift and drag.
© 2008 Elsevier Ltd. All rights reserved.

Keywords: Immersed-boundary method; Frequency effects; Oscillating cylinder; Lift and drag

1. Introduction

In this study, unsteady fluid dynamic simulations are implemented for flow/cylinder interactions to determine how oscillation frequencies of the cylinder influence lift and drag. In particular, flow across a transversely oscillating cylinder is modeled. The result is an effective representation of flow-structure and wave-structure interactions for many applications of flow and acoustic problems related to flow over bluff bodies, as well as for noise reduction analysis in measurement microphones [e.g., Zheng and Tan (2003)]. In fact, several research groups have concentrated on measurement of the near wake of an oscillating cylinder and the related vortex–structure interactions [e.g., Bishop and Hassan (1964), Griffin (1971), Ongoren and Rockwell (1988), Carberry et al. (2001), Williamson and Roshko (1988), and Krishnamoorthy et al. (2001)]. Detailed mechanisms have also been reviewed in classic articles such as those of Sarpkaya (1979), Bearman (1984), Parkinson (1989), Oertel (1990) and Zdravkovich (1997). Furthermore, new developments in numerical schemes for computational studies of flow over a two-dimensional oscillating cylinder have been recently reported in, for example, Blackburn and Henderson (1999), Anagnostopoulos (2000), and Guilmineau and Queutey (2002).

Ultimately, researchers have found that when the oscillation frequency (f) is near the natural von Karman vortex shedding frequency (f_s) of a corresponding stationary cylinder, frequency synchronization occurs. During this fundamental frequency lock-in, the vortex shedding is entrained by the cylinder motion; hence the vortex shedding

---

*Corresponding author. Tel.: +1 785 5325610; fax: +1 785 5327057.
E-mail address: zzheng@ksu.edu (Z.C. Zheng).

frequency changes to match the cylinder oscillation frequency. Furthermore, the frequency boundaries for frequency synchronization are dependent on oscillation amplitude, flow Reynolds number, and flow turbulence level. On the other hand, when f is appreciably different from f_s, complex wave forms contain beats, and several different frequencies can be produced. This is because the forces on the cylinder are affected by the free fluctuations of the wake and the forced oscillation of the wake. In addition, n-superharmonic synchronization (or frequency demultiplications, as named by Bishop and Hassan (1964)) and $1/n$-subharmonic synchronization can occur if f is approximately equal to an integer multiple or division of f_s, i.e., when $f = nf_s$ or $f = f_s/n$. Under these conditions, the wake still can be entrained to oscillate at a frequency close to f_s.

The purpose of this paper is to investigate how these frequencies influence the lift and drag of the oscillating cylinder. While the physical processes of formation of the near wake of an oscillating cylinder have been thoroughly investigated in the above-mentioned literature, to the authors' knowledge, detailed analyses of how fluid dynamic mechanisms related to wake vortex shedding influence the spectral contents of lift and drag have not been fully revealed. Consequently, an immersed-boundary method is used in this study that enables the simulation of flow over an oscillating cylinder to be carried out in a non-moving Cartesian grid with a stationary coordinate system. Ultimately, many of the simulated flow features in this study agree with the experimental findings in the literature, whereas the spectral analysis clearly provides further explanations of the flow physics for frequency responses of lift and drag in the frequency domain.
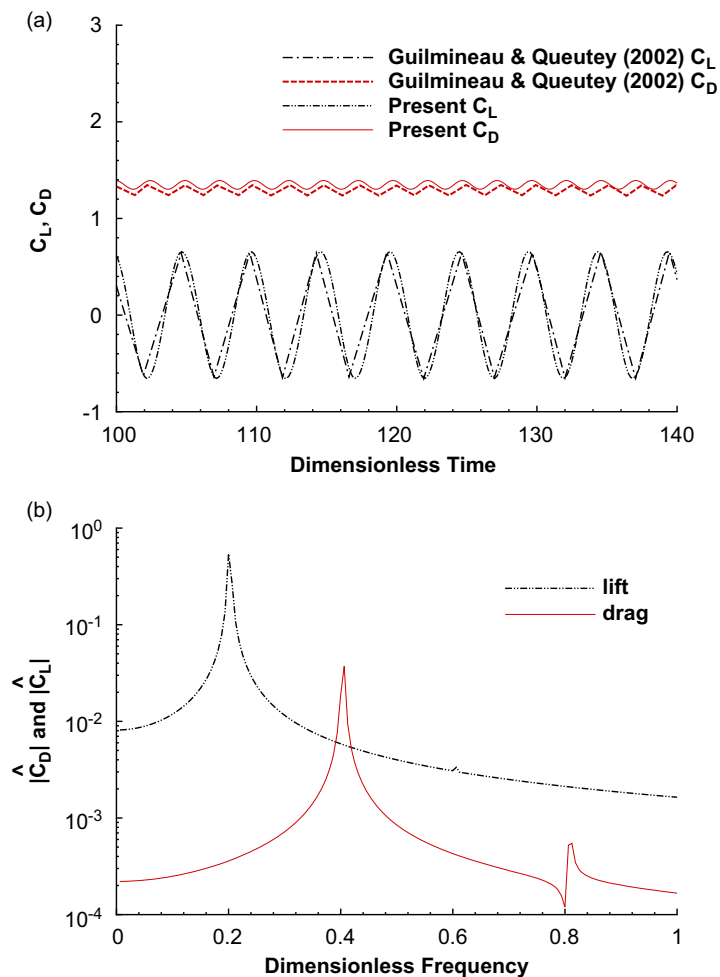
Fig. 1. The drag and lift coefficients of a stationary cylinder at Re = 200. (a) Comparisons of the time histories of the present computation with those of Guilmineau and Queutey (2002); (b) spectra of C_L and C_D.

2. Computation schemes

An immersed-boundary method with a direct compensation force (Zhang and Zheng, 2007), an improvement over those schemes described in Goldstein et al. (1993), Saiki and Biringen (1996), and Mohd-Yusof (1996), has been implemented to compute the fluid flow. In the immersed-boundary method, a forcing term is added to the
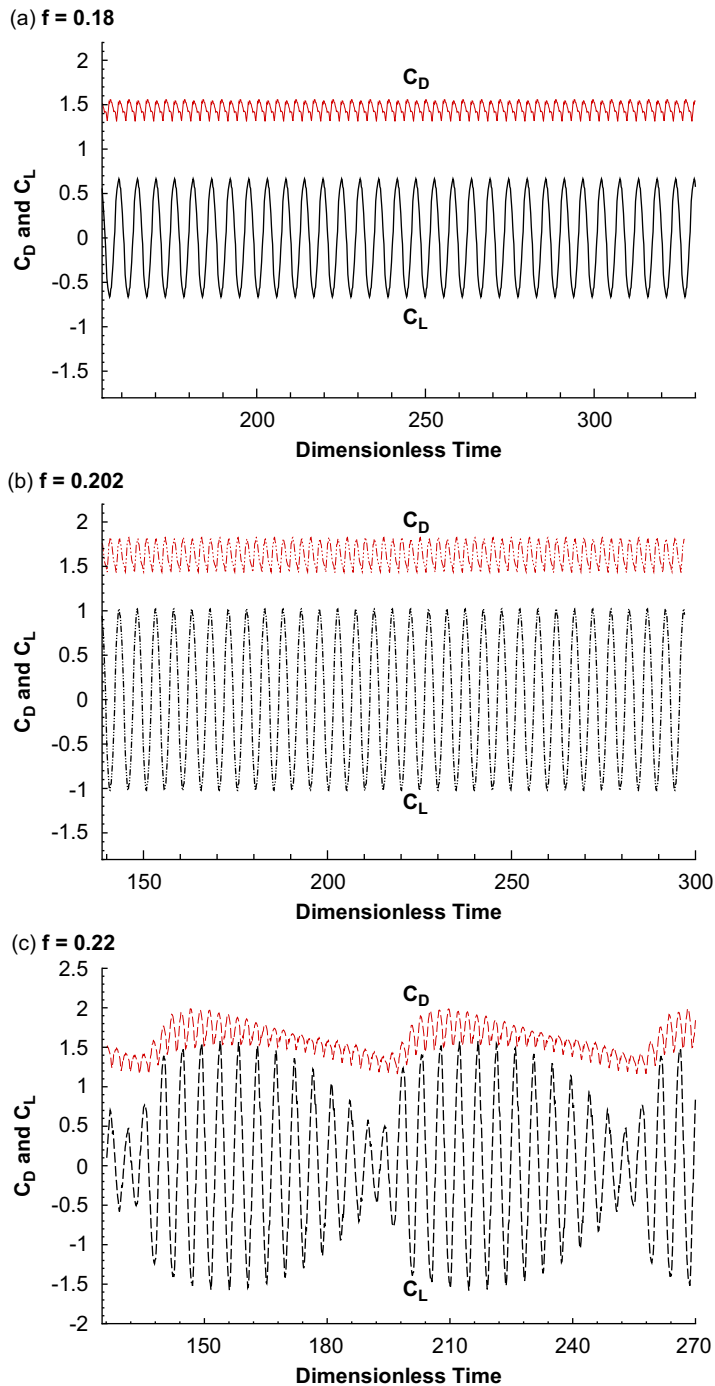
Fig. 2. Time histories of C_L and C_D for the frequency lock-in cases of (a) $f = 0.18$, (b) $f = 0.202$ and (c) $f = 0.22$.

Navier–Stokes equations to replace the boundary effects that move with the fluid and exert forces on it. There are two reasons for using the immersed-boundary method: (i) a simple Cartesian grid mesh can be used and there is no need to put body-fitted grids near the cylinder surface and (ii) moving grids or non-inertial coordinates to accommodate the motion of the oscillating cylinder are unnecessary in this method.

In the computation, nondimensionalization is characterized with the uniform incoming-flow speed, U, and the diameter of the cylinder, D. With the immersed-boundary method, the nondimensional equations for incompressible fluid flow are

$$\frac{\partial \mathbf{u}}{\partial t} + \mathbf{u} \cdot \nabla \mathbf{u} = -\nabla P + \frac{1}{\text{Re}} \nabla^2 \mathbf{u} + \mathbf{f} \tag{1}$$

and

$$\nabla \cdot \mathbf{u} = 0, \tag{2}$$

where $\mathbf{f}$ is the body force representing the boundary force. The forcing term $\mathbf{f}$, which functions as a velocity corrector for the grid points immediately inside the immersed boundary, is prescribed at each time step to establish the desired boundary moving velocity. For a time-marching scheme, this force can be expressed as

$$\mathbf{f} = \mathbf{S} + \nabla P - \frac{1}{\text{Re}} \nabla^2 \mathbf{u} + \frac{1}{\Delta t} (\mathbf{v} - \mathbf{u}) \tag{3}$$
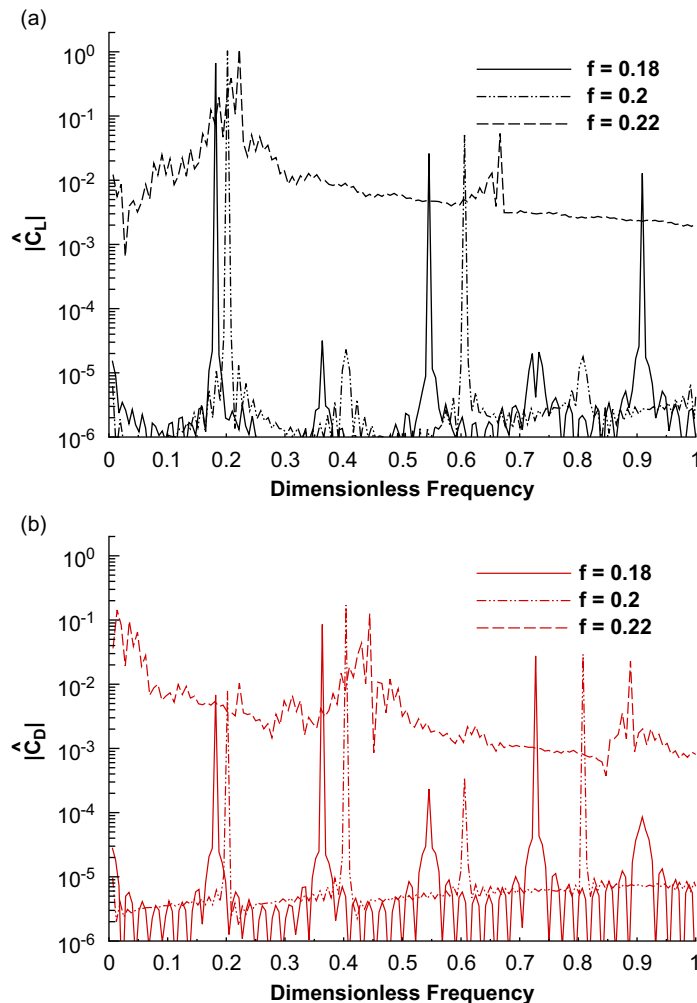
Fig. 3. Spectra of C_L and C_D for the frequency lock-in cases of $f = 0.18$, $f = 0.202$ and $f = 0.22$: (a) C_L spectra and (b) C_D spectra.

on the boundary, and zero elsewhere, and **S** is the convection term defined as:

$$\mathbf{S} = (\mathbf{u} \cdot \nabla)\mathbf{u}. \tag{4}$$

In Eq. (3), **v** is the desired velocity on a layer of grid points immediately inside the immersed boundary named the internal layer on which the direct forcing is applied to. More detailed explanations of the concept of immersed-boundary methods can be found in Zhang and Zheng (2007).

The unsteady, two-dimensional incompressible flow equations, Eq. (1), are solved using a second-order finite volume scheme on a staggered Cartesian grid. Continuity is enforced by solving a Poisson equation for pressure using a Poisson solver (Swarztrauber and Sweet, 1979). Given that the time-marching scheme is treated as a two-step predictor–corrector procedure, the convection terms are discretized using the second-order Adams–Bashforth method, and the diffusion terms are discretized using the second-order central differencing. In addition, with suggestions from Saiki and Biringen (1996), the normal direction diffusion terms are advanced implicitly using the Crank–Nicolson scheme.
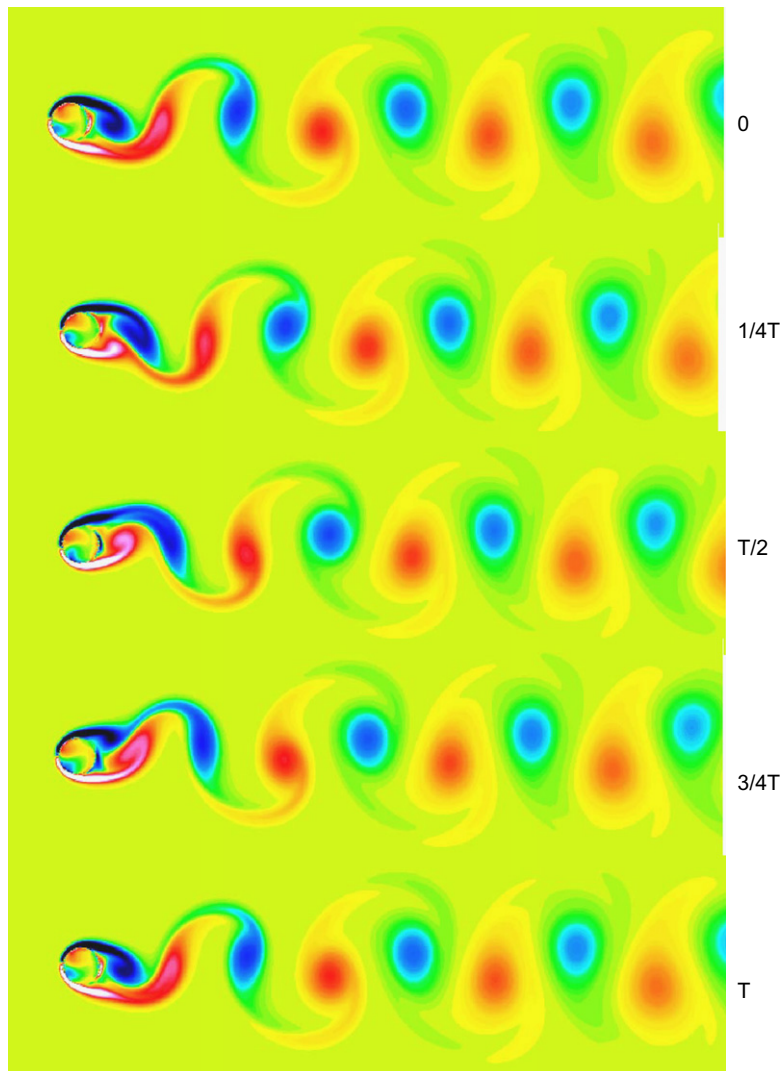
Fig. 4. Snapshots of vorticity contours for a frequency lock-in case of $f = 0.202$.

Only a simple arrangement of the computational grids is necessary because of the immersed-boundary method employed. In this study, a uniform Cartesian grid mesh is used, such that $\Delta x = \Delta y = 0.025$ in all of the computational cases. In the process of selecting grid size, the grid-size independence test was performed for the stationary cylinder case to determine the resolution using 0.05, 0.025 and 0.0125. The detailed grid-independence study was presented in a previous publication (Zhang and Zheng, 2007). The finest grid solution is regarded as "exact," and the errors of the solution are computed on the coarser grids. When changing the resolution, the L_2-norm of errors shows a -2 slope in the log–log plot of the norm versus the grid number. This means the overall computational accuracy is second order in space. The L_2-norm for the grid size of 0.025 is approximately 2×10^{-4}. Based on these test results, the grid size of 0.025 was thus selected, and the computation was performed on a staggered grid mesh. Finally, the domain size, 38.4×25.6, was tested to assure an independent solution to domain size. Accordingly, the center of the cylinder is located at 8 from the inlet, which is sufficient to avoid inlet boundary effects (Ravoux et al., 2003), and 12.8 from the top or bottom boundary.
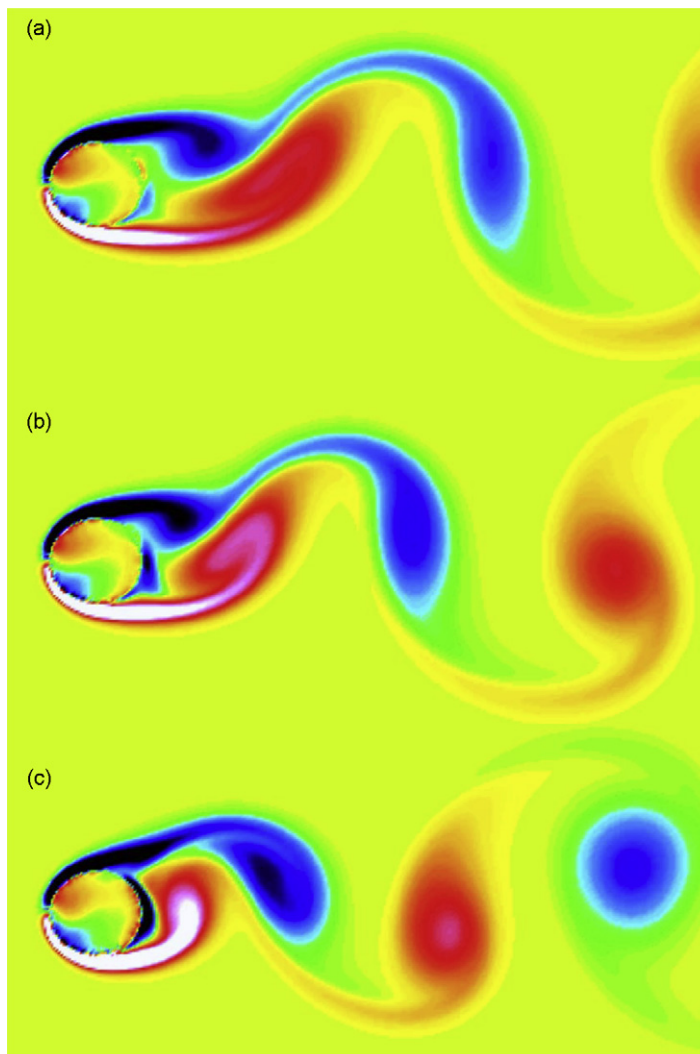
Fig. 5. Snapshots of vorticity contours for the flow around the oscillating cylinder at the moment when the center of the cylinder is located at the maximum negative displacement of the cylinder, for the three frequency lock-in cases: (a) $f = 0.18$, (b) $f = 0.202$ and (c) $f = 0.22$.

The stability analysis of the scheme yields a stability criterion that is no more restrictive than that of an explicit scheme for a two-dimensional convection–diffusion equation

$$\delta t < \min \left[\frac{h^2 \text{Re}}{4}, \frac{2}{(u^2 + v^2)\text{Re}} \right], \tag{5}$$

where h is the grid size. The first part in the minimum function concerns diffusion, while the second part is the Courant number related to convection. Clearly, the dimensionless time step used in the computation has to satisfy the stability condition imposed by Eq. (5) for the Reynolds number and the grid size used in this study. In addition, a more restrictive condition in selecting the time-step size is to capture sufficiently high frequency phenomena in the flow. With these two conditions, the time-step size in the computation is thus selected to allow at least 512 time steps in each oscillation period corresponding to the oscillation frequency.

In the current study, the oscillation in the transverse direction has the dimensionless displacement of

$$d_y = A \sin(2\pi t * f), \tag{6}$$

where A is the dimensionless amplitude of the oscillating displacement (normalized by the diameter of the cylinder D), and f is the dimensionless oscillation frequency. The motion described in Eq. (6) is applied to all the immersed boundary points (i.e., all the points on the cylinder surface), and there is no motion in x direction on the cylinder surface.

The fidelity of the computation scheme has been verified with numerous experimental and computational data in the literature for flows over cylinders and spheres (Zhang and Zheng, 2007). Particularly, the computational results of fluctuation quantities of flow over an oscillating cylinder have been compared with experimental data by Griffin (1971) at Re = 200 on several r.m.s. velocity-fluctuation profiles, and a very good agreement between the two results has been achieved, as shown in Zhang and Zheng (2007). Another example for comparison with literature data is shown in Fig. 1(a), where the time histories of drag and lift coefficients, C_D and C_L, in the case of a stationary cylinder of the present computation are compared with those of Guilmineau and Queutey (2002) at Re = 200, which provides further evidence that the current computational result agrees with others.
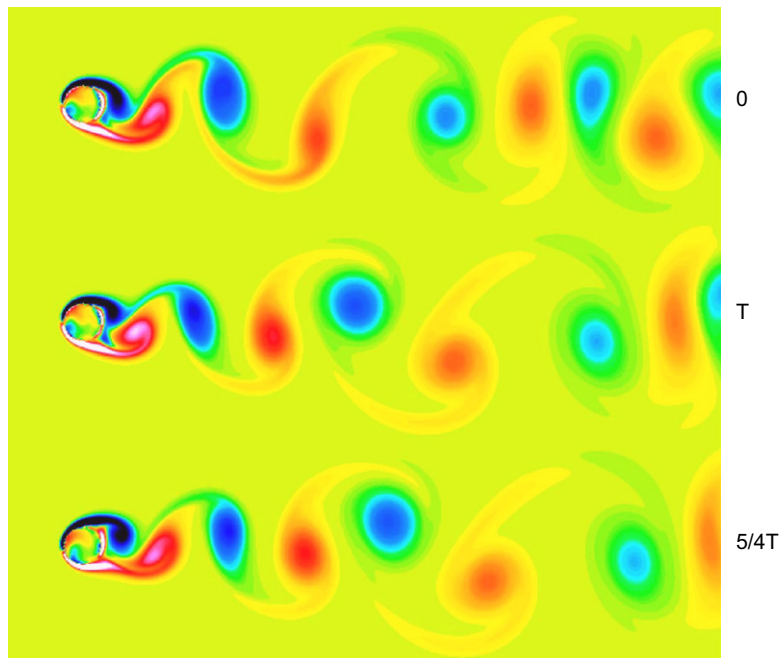
Fig. 6. Snapshots of vorticity contours for the non-synchronization case of $f = 0.25$.

3. Analysis of frequency effects

The subsequent analysis is based on the computational results of the lift and drag coefficients determined by

$$C_D = \int_0^{2\pi} p \cos\theta \, d\theta - \frac{2}{Re} \int_0^{2\pi} \frac{\partial u}{\partial x} \cos\theta \, d\theta + \frac{1}{Re} \int_0^{2\pi} \left(\frac{\partial u}{\partial y} + \frac{\partial v}{\partial x} \right) \sin\theta \, d\theta \tag{7}$$

and

$$C_L = - \int_0^{2\pi} p \sin\theta \, d\theta - \frac{1}{Re} \int_0^{2\pi} \left(\frac{\partial u}{\partial y} + \frac{\partial v}{\partial x} \right) \cos\theta \, d\theta + \frac{2}{Re} \int_0^{2\pi} \frac{\partial v}{\partial y} \sin\theta \, d\theta, \tag{8}$$

where θ starts from the front center on the cylinder surface and increases clockwise. In this study, the desired frequency range corresponds to a dimensionless frequency (f) range of 0.1–1, characterized by the inflow speed and cylinder diameter. This range includes $\frac{1}{2}$-subharmonics and up to 5-superharmonics of the natural von Karman vortex shedding frequency near $f_s = 0.2$. Therefore, in the following cases, the oscillation frequency is ranged to include $\frac{1}{2}$-subharmonics ($f/f_s \approx 0.5$), fundamental synchronization ($f/f_s \approx 1$), 1.5-superharmonics ($f/f_s \approx 1.5$) and 2- and 3-superharmonics ($f/f_s \approx 2$ and 3). The presented spectra are FFTs of the time history of C_D and C_L fluctuations. For each case, time-history data of 30 periods (the $\frac{1}{2}$-subharmonic $f = 0.1$ case), 60 periods (the other oscillation cases), or 90 periods (the
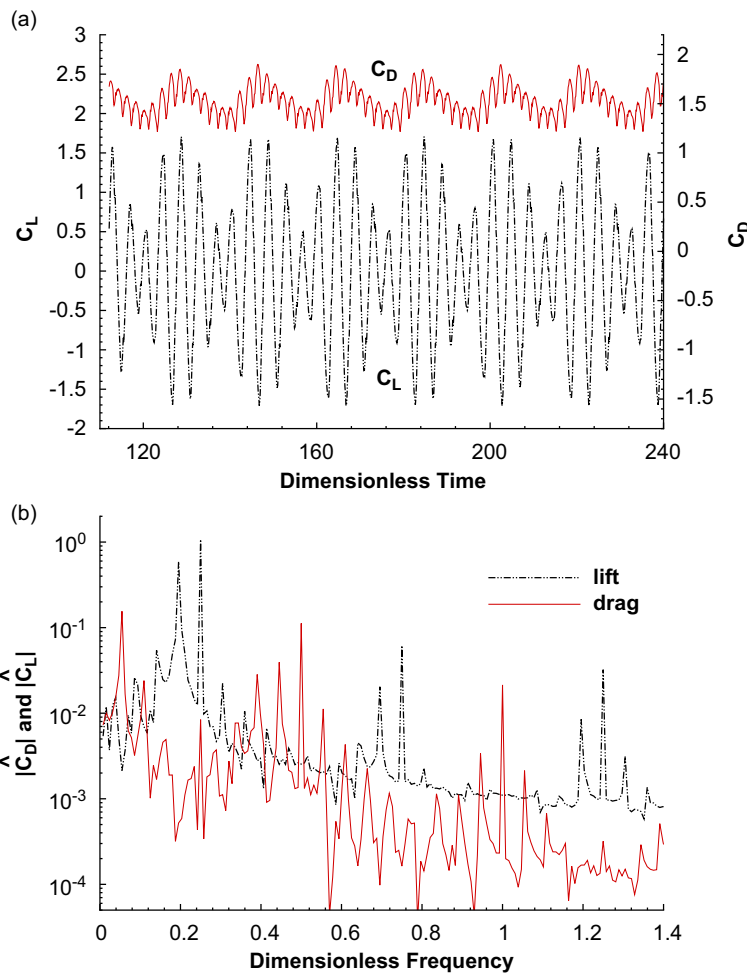
Fig. 7. C_L and C_D for the non-synchronization case of $f = 0.25$: (a) time histories and (b) spectra.

stationary case) are simulated. The FFT is performed using the data in the last 16 periods (of 30 periods) or the last 32 periods (of 60 periods) or the last 64 periods (of 90 periods), and therefore the spectral resolution is from 0.003125 (the stationary case) to 0.01875 (the $f = 0.6$ case) dimensionless frequency units.

In the following simulation cases, the Reynolds number is fixed at 200, and the mean component was already subtracted out in all the spectra shown in the paper. To begin, the case of a stationary cylinder was first simulated to determine the natural frequency of vortex shedding. The result, as presented in Fig. 1(b), shows a dominant peak in the C_L spectrum at 0.202, while a peak at 0.404 exists in the C_D spectrum. This proves that in the present simulation, the natural vortex shedding frequency for flow over a stationary cylinder at Re = 200 is 0.202. The resolution in determining the natural vortex shedding frequency is enhanced by adding zeros to the time-series data. In all the oscillating cylinder cases, the amplitude for the oscillation, A in Eq. (6), has been fixed at 0.15, except for one case with $A = 1$ at $f = 0.1$.

3.1. Fundamental frequency lock-in

The study presents three cases of fundamental frequency synchronization, and the oscillation frequencies, f, for the cases of 0.18, 0.202 and 0.22, are near the natural vortex shedding frequency of 0.202. Figs. 2 and 3 are the time histories
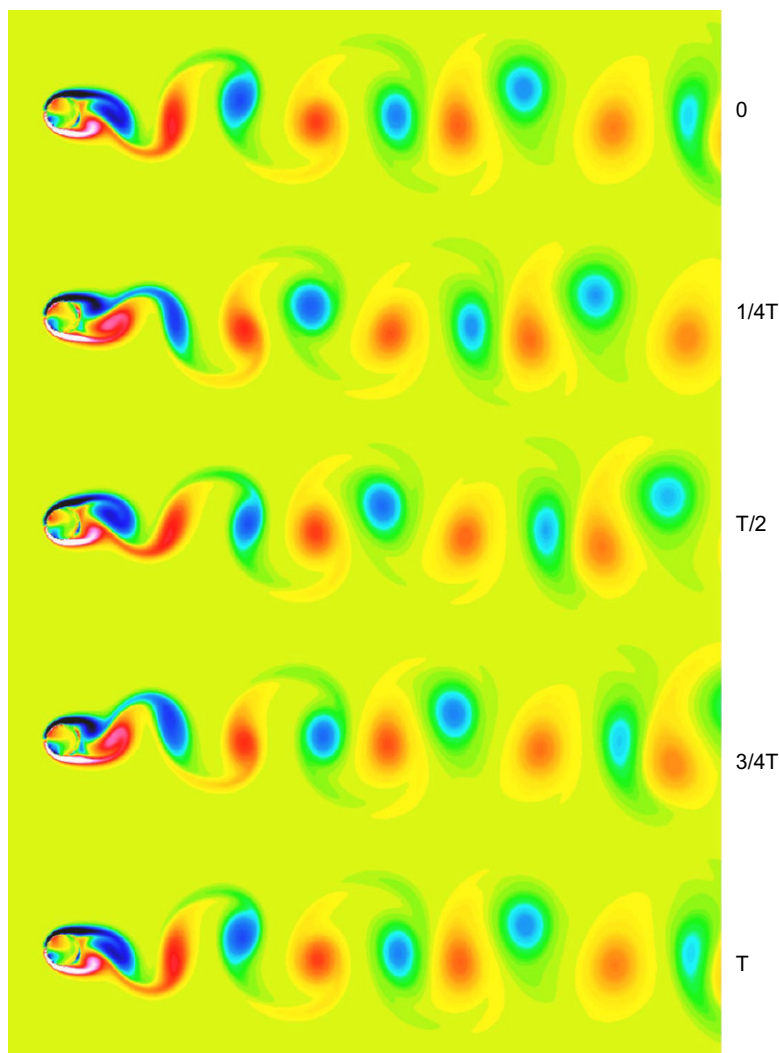
Fig. 8. Snapshots of vorticity contours for $\frac{1}{2}$-subharmonic excitation of $f = 0.1$ and $A = 0.15$.

and fluctuation spectra of C_L and C_D for these three cases. In this frequency range, the simulated flowfield reveals the same 2S vortex wake structures shown in Fig. 4 for $f = 0.202$, as those demonstrated in the experiments by Ongoren and Rockwell (1988), Williamson and Roshko (1988) and Krishnamoorthy et al. (2001). The term 2S means two single vortices are shed at each cylinder oscillation cycle, as first determined by Williamson and Roshko (1988). Noticeably, there is flow both inside and outside the cylinder, since the immersed-boundary method computes the flow on the entire Cartesian grid without regard to the location of the physical boundary of the body. The flow structures clearly indicate that frequency lock-in occurs; this means the dominant vortex shedding frequency shifts to f. Therefore, both the time history and the spectrum of C_L show a dominant frequency at f in each case in Figs. 2 and 3. The lowest peak frequency in the C_D spectrum is $2f$, because the drag is dominated by the wake vortex shedding, which creates two vortices in each oscillation cycle. Ostensibly in all three cases, while the C_L spectrum has narrow-band peaks in 1, 3 and 5 harmonics, the C_D spectrum has peaks in 2 and 4 harmonics.

In the time histories of the $f = 0.22$ case in Fig. 2(c), there is a clear beat both in C_L and C_D, and the frequency of the beat of 0.02 is the largest common factor of 0.2 and 0.22. This kind of beats also showed in the time-history simulations by Guilmineau and Queutey (2002) at the frequency ratio of $f/f_s = 1.1$, and did not show in any case where the ratio was less than 1. Also, the relative magnitude of the beat, in comparison to the oscillating magnitude, is larger in C_D than in C_L. This results in a significant high amplitude of the C_D spectrum at the low frequency near 0.02 in Fig. 3(b).
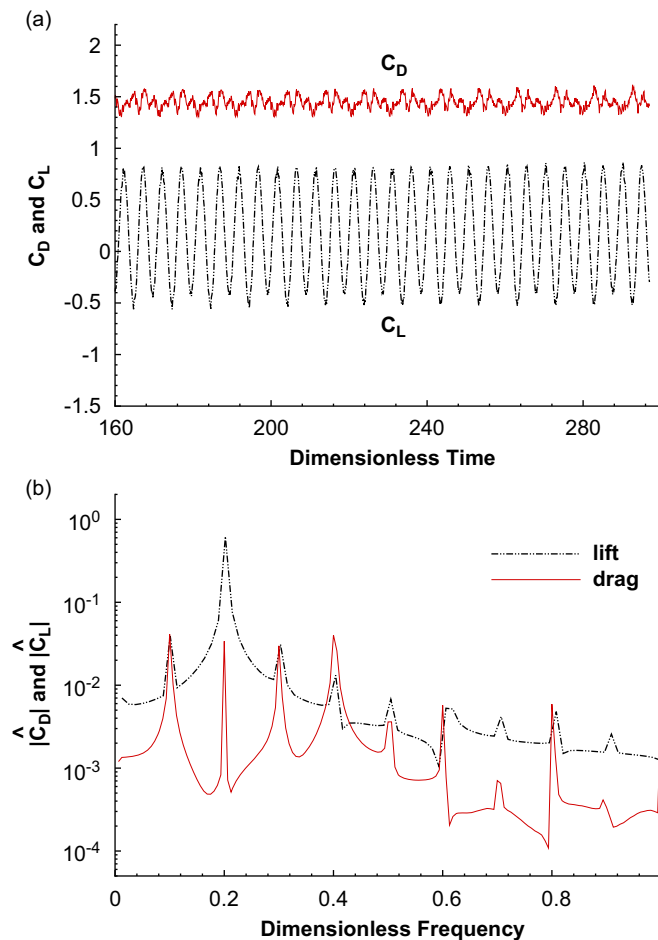
Fig. 9. C_L and C_D for $\frac{1}{2}$-subharmonic excitation of $f = 0.1$ and $A = 0.15$: (a) time histories and (b) spectra.

The $f = 0.18$ and 0.202 cases are examples of phase-locking synchronization when vortex shedding is in-phase with the cylinder oscillation. The $f = 0.22$ case is out-of-phase synchronization when the phase of vortex shedding is π different from that of cylinder oscillation. Fig. 5 shows the vorticity contours (of the component perpendicular to the paper surface) near the cylinder for these three cases. At the moment of the snapshot of these contours, the center of the cylinder is located at the maximum negative displacement of the cylinder. Clearly at this moment, a vortex sheds from the bottom of the cylinder in the $f = 0.22$ case, while a vortex sheds from the opposite side in the other two cases. Ongoren and Rockwell (1988) also observed this in their experiment in the frequency range of $0.85 \leqslant f/f_s \leqslant 1.17$. Approaching $f/f_s = 1$, there is substantial shortening of the vortex length, and just above this frequency ratio, a switch occurs in the phase of vortex shedding to the opposite side of the cylinder. The described vortex structure is clearly shown in Fig. 5. In addition, the $f = 0.22$ case locates almost at the margin of the frequency range of fundamental synchronization, according to the experimental data in the above-mentioned literature. The closeness to out-of-phase synchronization may be attributable to the characteristics not seen in the other two synchronized cases: a wider noise band around the peaks, particularly near f in the C_L spectrum, and near $2f$ in the C_D spectrum.
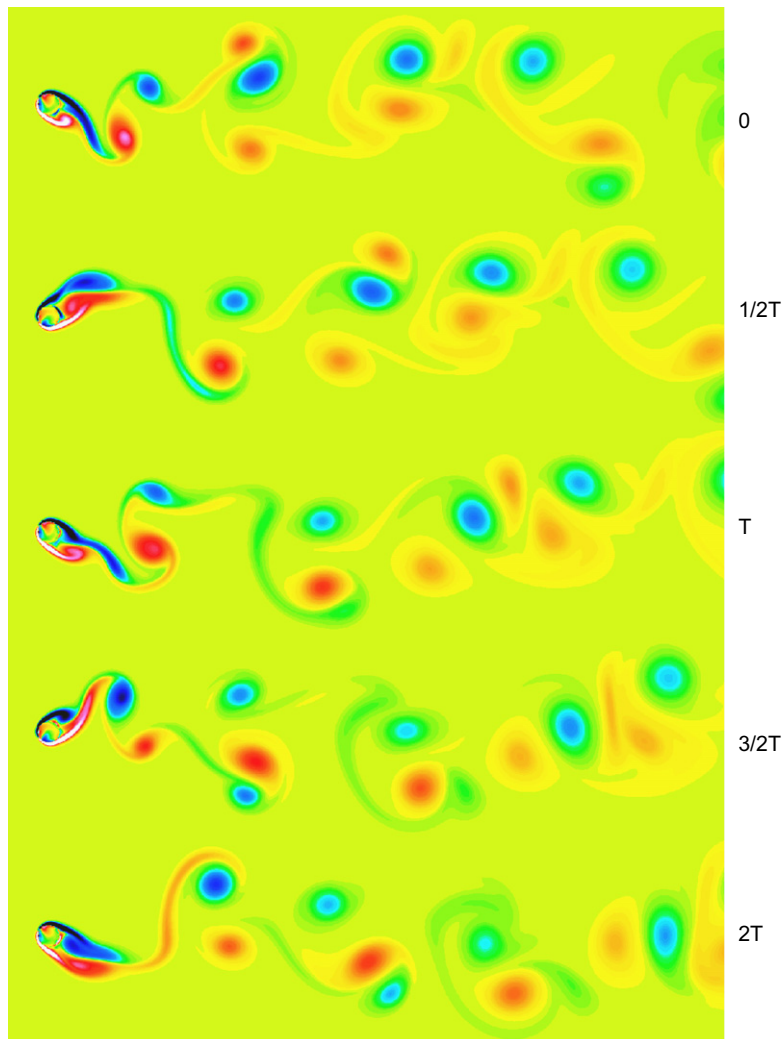
Fig. 10. Snapshots of vorticity contours for $\frac{1}{2}$-subharmonic excitation of $f = 0.1$ and $A = 1.0$.

Since $f = 0.22$ reaches the margin of the frequency range of fundamental synchronization, further increase of the oscillation frequency causes non-synchronization. Fig. 6 shows vorticity contours and Fig. 7 shows the time histories and the spectra of C_L and C_D for the $f = 0.25$ case. The non-synchronization flow structure in Fig. 6 shows that the near-wake resembles periodicity both after one period (T) with respect to $f = 0.25$ and also after $5T/4$ because $f_s = 0.2$. This is also clearly shown in C_L spectrum in Fig. 7(b) where, instead of only one peak frequency in the lock-in cases, two dominant frequencies at 0.25 and 0.2 correspond to the oscillation frequency and the natural vortex shedding frequency, respectively. In C_D spectrum, two peaks, each at twice the peak frequencies in C_L spectrum, can be observed. However, because of the multiple peaks with non-synchronization, these peak levels are less significant than those in the synchronized cases. Finally, the beat, similar to that in the time history of the $f = 0.22$ case, is shown in this case too, which results in a clear peak at the frequency of 0.05 in C_D spectrum.

3.2. $\frac{1}{2}$-subharmonic excitation

An oscillation frequency of $f = 0.1$ is studied for this case, and at this frequency four vortices are shed from the cylinder during each oscillation cycle, as shown in Fig. 8. Williamson and Roshko (1988) did not find synchronization pattern at the $\frac{1}{2}$-subharmonic oscillation. However, both Ongoren and Rockwell (1988) and Krishnamoorthy et al. (2001) showed synchronization at this frequency. This is probably because of the smaller oscillation amplitude in the latter two studies ($0.13D$ and $0.22D$, respectively) than in the former one ($> 1.0D$). The asymmetric vortex shedding
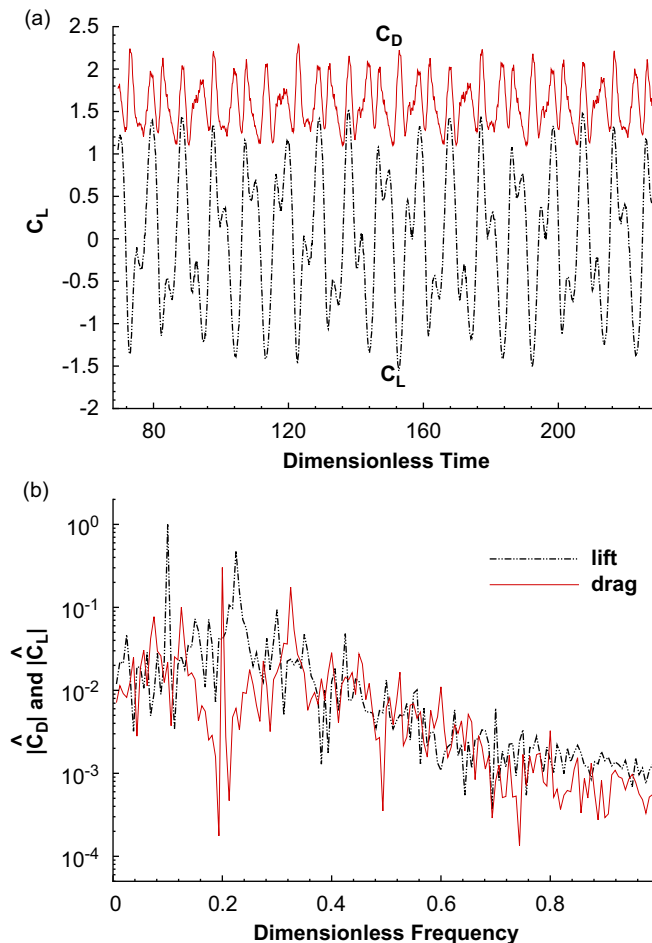
Fig. 11. C_L and C_D for $\frac{1}{2}$-subharmonic excitation of $f = 0.1$ and $A = 1.0$: (a) time histories and (b) spectra.
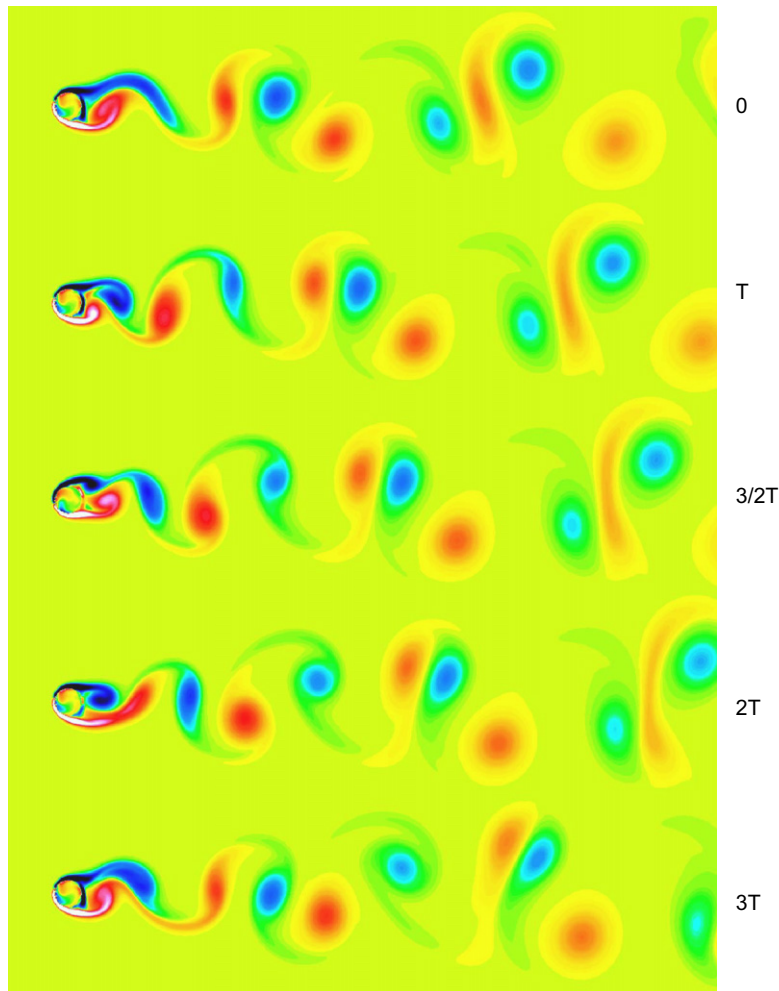
Fig. 12. Snapshots of vorticity contours for 1.5-superharmonic excitation of $f = 0.3$.

pattern described in Williamson and Roshko (1988) is not significant when the oscillation amplitude is small, and therefore a symmetric synchronization still shows in Ongoren and Rockwell (1988) and Krishnamoorthy et al. (2001). In the case studied here, since the amplitude is $0.15D$, the flow behaves more like that observed by Ongoren and Rockwell (1988) and Krishnamoorthy et al. (2001). In Fig. 8, the flow structure resemblance occurs at every $T/2$, corresponding to the natural vortex shedding frequency of $f_s = 2f = 0.2$, although more complete periodicity is at every T. Fig. 9(b) shows a significant peak exists at $f_s = 0.2$ in the C_L spectrum and at $2f_s$ in the C_D spectrum, which is an evidence of synchronization. The significant peak at the oscillation frequency itself ($f = 0.1$) in C_D spectrum, with peaks also at the super-harmonics of 0.1, is due to incomplete synchronization, following a wake vortex pattern at the oscillation frequency itself as shown in Fig. 8.

To test the amplitude effect, cases with different amplitudes were simulated with $A = 0.13$, 0.15, 0.25, 0.5 and 1. When A increases, periodicity per half-cycle (corresponding to the natural shedding frequency) is gradually lost, and at $A = 1$, non-synchronization is observed. This result supports the statement made above about the effect of amplitude. The $A = 1$ result is shown in Figs. 10 and 11. In Fig. 10, it can be seen that the wake structure is not quite periodic after one cycle of cylinder oscillation, and that vortex shedding does not repeat every half-cycle of cylinder displacement. The wake structure is not symmetric, which agrees to what is indicated in the work of Williamson and Roshko (1988), although the 2P structure as illustrated in their paper does not show in Fig. 10. In Fig. 11, while there is still a peak at the oscillation frequency itself, there is only a small peak that is shifted away from the natural shedding frequency, and therefore no synchronization exists.
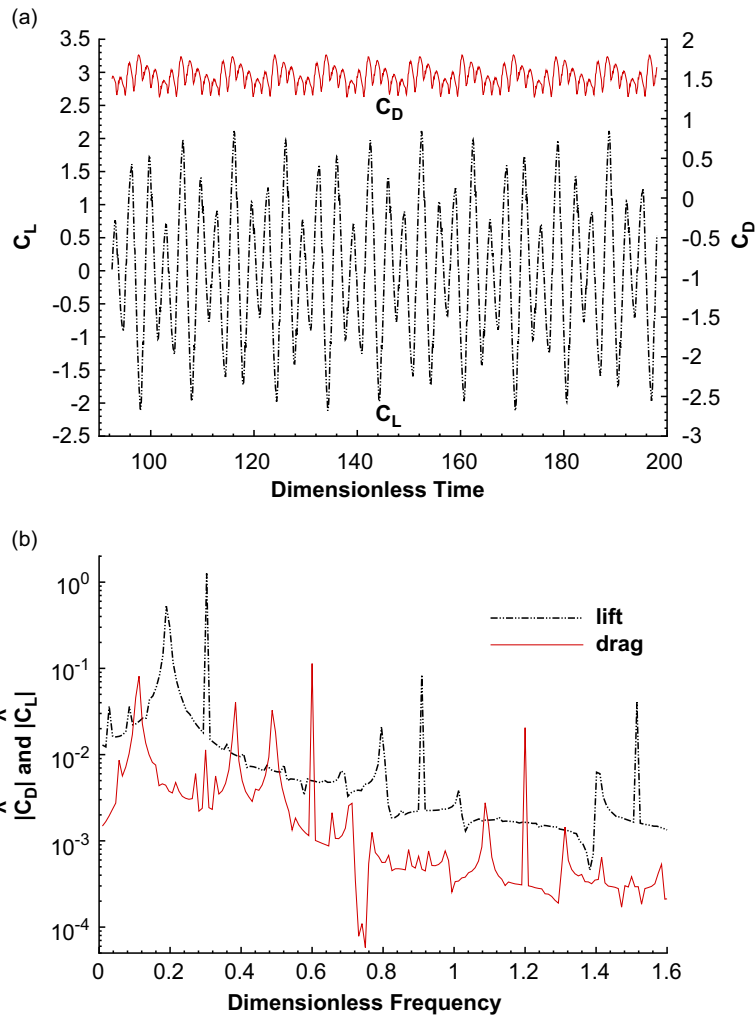
Fig. 13. C_L and C_D for 1.5-superharmonic excitation of $f = 0.3$: (a) time histories and (b) spectra.

3.3. 1.5-superharmonic excitation

Next, a 1.5-superharmonic excitation case is studied at $f = 0.3$. At this frequency, both of the experiments by Ongoren and Rockwell (1988) and Krishnamoorthy et al. (2001) found that the primary vortex shedding frequency is still the natural shedding frequency, close to $f_s = 0.2$. While no obvious synchronization was found at this frequency, the simulation in this study, as well as the measurement in these two experiments, shows a large-amplitude coherent component at $f/3 = 0.1$ that repeats every three cycles of oscillation. This flow structure can be seen in vorticity contours in Fig. 12 where the flow resemblance shows after $3T$. This can also be seen in the time histories and fluctuation spectra in Fig. 13. In C_L spectrum, dominant peaks are at both 0.2 (f_s) and 0.3 (f), showing non-synchronization. In C_D spectrum, a strong peak at 0.1 ($f/3$) occurs that is related to the $f/3$ large-amplitude structure. Correspondingly, peaks at 0.4 ($2f_s$), 0.5, and 0.6 ($2f$) appear in C_D spectrum. Another significant peak at 1.2 is caused by the superharmonics of both 0.4 and 0.6.

3.4. 2- and 3-superharmonic excitation

With the 2- or 3-superharmonic excitation, a complex wave-form composed of two simple components with a frequency ratio of $\frac{1}{2}$ or $\frac{1}{3}$ can be distinguished, which can be seen clearly in the time history of C_L in Figs. 14 and 15 for
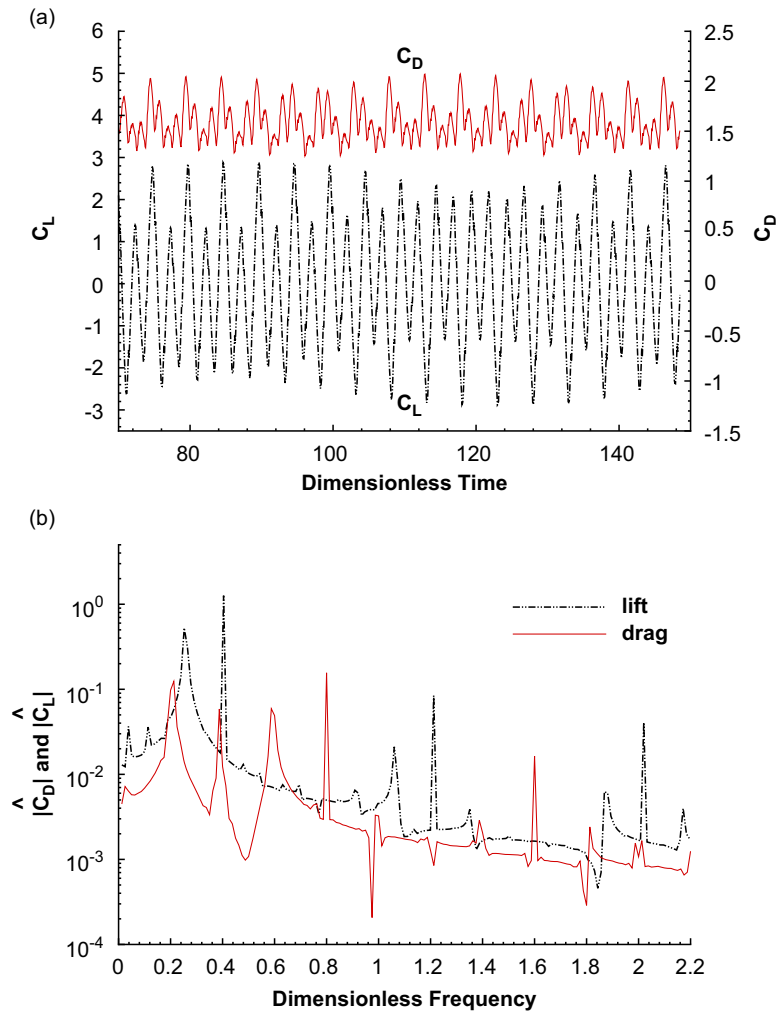
Fig. 14. C_L and C_D for 2-superharmonic excitation of $f = 0.4$: (a) time histories and (b) spectra.

$f = 0.4$ and $f = 0.6$, respectively. Every complete cycle of the entrained frequency of natural vortex shedding contains exactly 2 or 3 cycles of the oscillation frequency, as shown in vorticity contours in Figs. 16 and 17. Therefore the wake pattern quickly relaxes to the usual von Karman mode. This frequency demultiplication, which occurs when the oscillation frequency is an integer multiple of the natural vortex shedding frequency, is related to the lift and drag force synchronization determined by Bishop and Hassan (1964). Based upon visualization and hot film experiments, Krishnamoorthy et al. (2001) pointed out that at the superharmonic excitation, the dynamics in the formation region is not synchronized to cylinder motion except for the 3-superharmonic synchronization. They claimed that during the 3-superharmonic excitation, the near-wake dynamics repeated itself every third cycle, and a coherent, synchronized wake pattern was formed. In our results, both the $\frac{1}{2}$-cycle coherence for the 2-superharmonic excitation and the $\frac{1}{3}$-cycle coherence for the 3-superharmonic excitation are demonstrated in Figs. 14 and 15. However, the specific difference of near-wake dynamics between the 2- and 3-superharmonics is not detected in the simulated flow visualization of this study as shown in Figs. 16 and 17. The C_L spectra in Figs. 14(b) and 15(b) show that in both cases there is a peak at the natural vortex shedding frequency at 0.2 and a peak at the fluctuation frequency (at 0.4 in Fig. 14(b) and 0.6 in Fig. 15(b)). However, C_D spectrum shows differences between the two cases. For instance, 3-superharmonic case shows significant peaks only at 0.4 ($2f_s$), 0.8 ($4f_s$) and 1.2 ($2f$), but 2-superharmonic case has peaks also at 0.2 (f_s) and 0.6 ($3f_s$), in addition to the peaks at the even-harmonic frequencies at 0.4 ($2f_s$) and 0.8 ($2f$). This means that
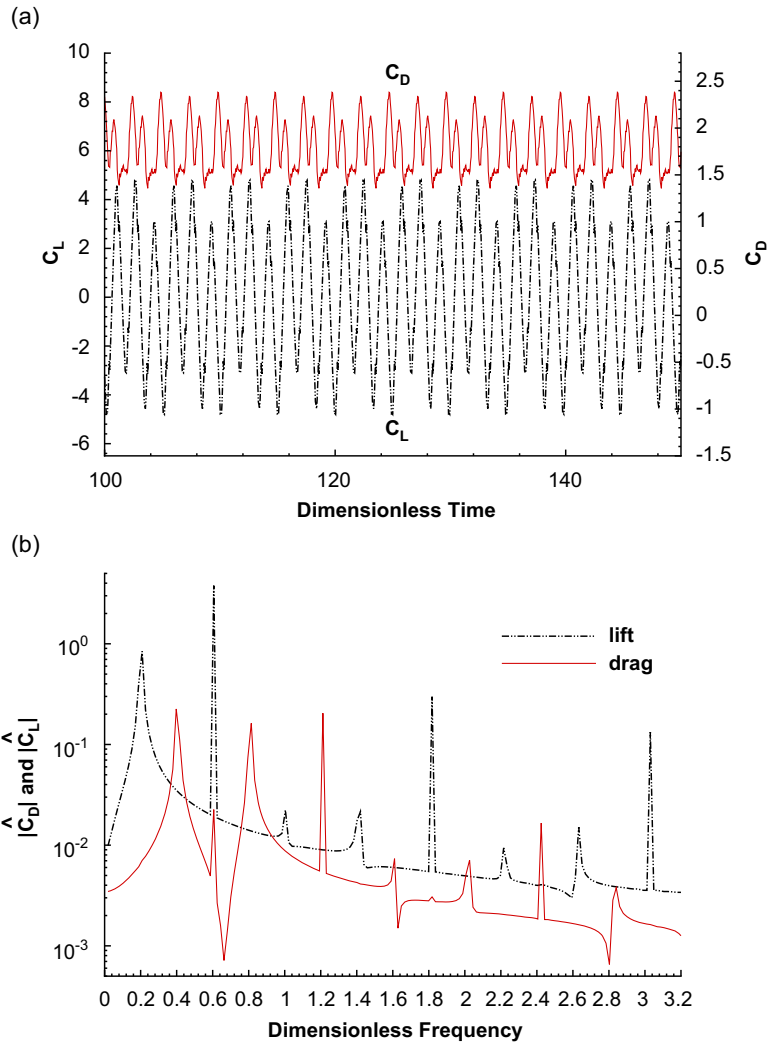
Fig. 15. C_L and C_D for 3-superharmonic excitation of $f = 0.6$: (a) time histories and (b) spectra.

2-superharmonic case is not as synchronized as 3-superharmonic case. Likely, this is because C_D spectrum is usually related to more subtle flow structure than C_L spectrum, as shown in several previous cases.

4. Conclusions

The simulated flow-field with subharmonic and superharmonic cylinder oscillations has been correlated with phenomena observed in fluid dynamics experiments in the literature. In some cases, high spectral-peak levels of C_L and C_D are observable due to the coupling between the oscillations and the natural vortex shedding. Also, near the natural frequency, frequency lock-in occurs, resulting in significant peaks in the spectra at f for C_L and at $2f$ for C_D. Next, away from the lock-in regime, both peaks at f and f_s for C_L and at $2f$ and $2f_s$ for C_D are visible. Then, at $\frac{1}{2}$-subharmonic excitation, both synchronization and incomplete synchronization exist at small oscillation amplitude, with peaks at f_s for C_L and at f for C_D. When the amplitude is large, no synchronization can be observed. Further, at the 1.5-, 2- and 3-superharmonic excitations, the frequency demultiplication leads to large-amplitude coherent components at fractions of the excitation frequencies. Finally, in all the superharmonic cases, while C_L spectrum shows peaks mostly at the natural frequency and the excitation frequencies, C_D spectrum has peaks at these fractions of the excitation frequencies.
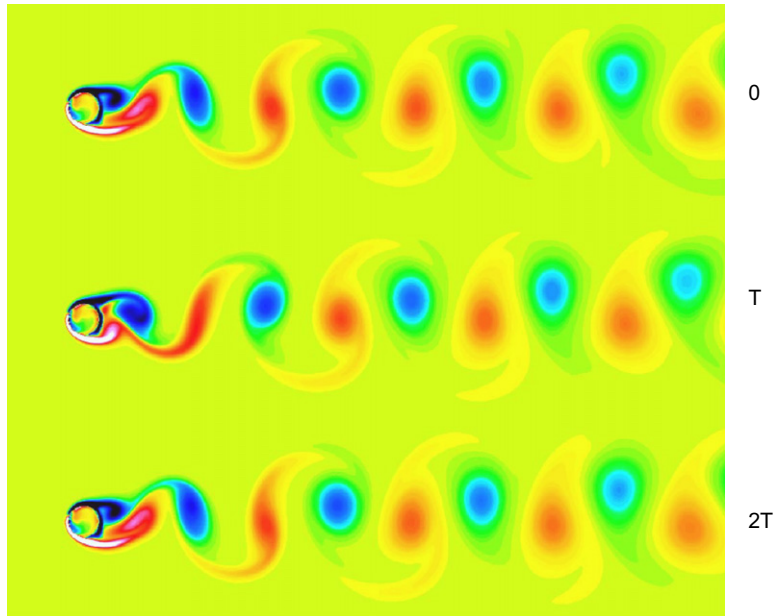
Fig. 16. Snapshots of vorticity contours for 2-superharmonic excitation of $f = 0.4$.
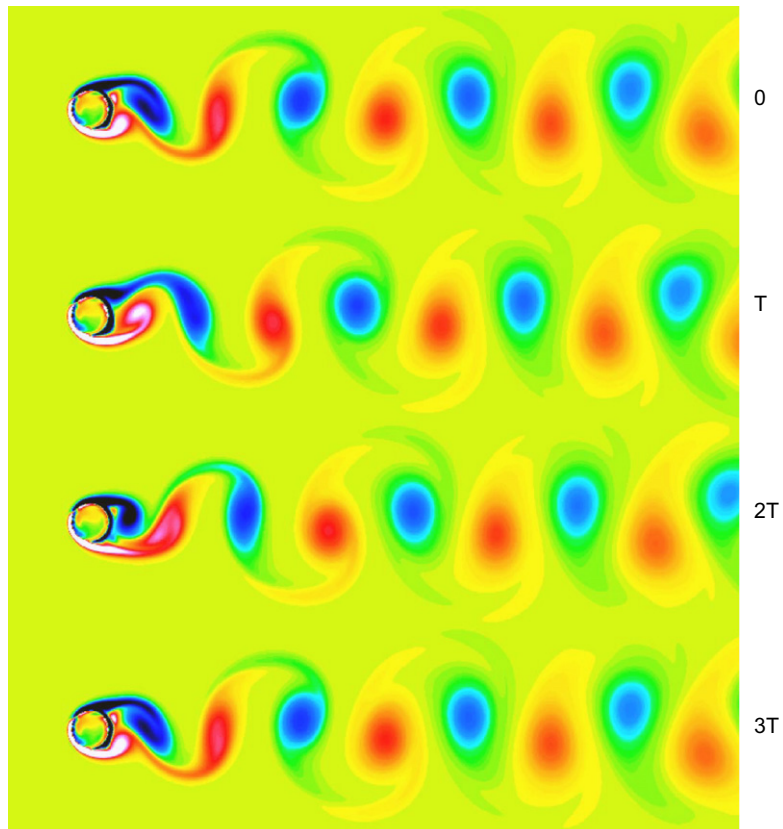
Fig. 17. Snapshots of vorticity contours for 3-superharmonic excitation of $f = 0.6$.

References

Anagnostopoulos, P., 2000. Numerical study of the flow past a cylinder excited transversely to the incident stream. Part 1: lock-on zone, hydrodynamic forces and wake geometry. Journal of Fluids and Structures 14, 819–851.

Bearman, P.W., 1984. Vortex shedding from oscillating bluff bodies. Annual Review of Fluid Mechanics 16, 195–222.

Bishop, R.E.D., Hassan, A.Y., 1964. The lift and drag forces on a circular cylinder oscillating in a flowing fluid. Proceedings of Royal Society of London A 277, 51–75.

Blackburn, H.M., Henderson, R.D., 1999. A study of two-dimensional flow past an oscillating cylinder. Journal of Fluid Mechanics 385, 255–286.

Carberry, J., Sheridan, J., Rockwell, D., 2001. Forces and wake modes of an oscillating cylinder. Journal of Fluids and Structures 15, 523–532.

Griffin, O.M., 1971. The unsteady wake of an oscillating cylinder at low Reynolds number. Journal of Applied Mechanics 38, 729–738.

Goldstein, D., Handler, R., Sirovich, L., 1993. Modeling a no-slip flow boundary with an external force field. Journal of Computational Physics 105, 354–366.

Guilmineau, E., Queutey, P., 2002. A numerical simulation of vortex shedding from an oscillating circular cylinder. Journal of Fluids and Structures 16, 773–794.

Krishnamoorthy, S., Price, S.J., Païdoussis, M.P., 2001. Cross-flow past an oscillating circular cylinder: synchronization phenomena in the near wake. Journal of Fluids and Structures 15, 955–980.

Mohd-Yusof, J., 1996. Interaction of massive particles with turbulence. Ph.D. Dissertation, Department of Mechanical and Aerospace Engineering, Cornell University, Ithaca, NY, USA.

Oertel Jr., H., 1990. Wakes behind blunt bodies. Annual Review of Fluid Mechanics 22, 539–564.

Ongoren, A., Rockwell, D., 1988. Flow structure from an oscillating cylinder. Part 1. Mechanisms of phase shift and recovery in the near wake. Journal of Fluid Mechanics 191, 197–223.

Parkinson, G.V., 1989. Phenomena and modeling of flow-induced vibrations of bluff bodies. Progress in Aerospace Science 26, 169–224.

Ravoux, J.F., Nadim, A., Haj-Hariri, H., 2003. An embedding method for bluff body flows: interactions of two side-by-side cylinder wakes. Theoretical and Computational Fluid Dynamics 16, 433–466.

Saiki, E.M., Biringen, S., 1996. Numerical simulation of a cylinder in uniform flow: application of a virtual boundary method. Journal of Computational Physics 123, 450–465.

Sarpkaya, T., 1979. Vortex-induced oscillations—a selective review. Journal of Applied Mechanics 46, 241–258.

Swarztrauber, P.N., Sweet, R.A., 1979. Algorithm 541, efficient FORTRAN subprograms for the solution of separable elliptic partial differential equations [D3]. ACM Transaction on Mathematical Software 5, 352–364.

Williamson, C.H.K., Roshko, A., 1988. Vortex formation in the wake of an oscillating cylinder. Journal of Fluids and Structures 2, 355–381.

Zdravkovich, M.M., 1997. Flow around Circular Cylinders. Oxford University Press, New York.

Zhang, N., Zheng, Z.C., 2007. An improved direct-forcing immersed-boundary method for finite difference applications. Journal of Computational Physics 221, 250–268.

Zheng, Z.C., Tan, B.K., 2003. Reynolds number effects on flow/acoustic mechanisms in spherical windscreens. Journal of Acoustical Society of America 113, 161–166.